ADVANCED MATERIALS INTERFACES
www.advmatinterfaces.de

Interface Thermal Resistance between Monolayer WSe_2 and SiO_2: Raman Probing with Consideration of Optical–Acoustic Phonon Nonequilibrium

Nicholas Hunter, Nurul Azam, Hamidreza Zobeiri, Nathan Van Velson, Masoud Mahjouri-Samani,* and Xinwei Wang**

This work explores the 2D interfacial energy transport between monolayer WSe_2 and SiO_2 while considering the thermal nonequilibrium between optical and acoustic phonons caused by photoexcitation. Recent modeling and experimental work have shown substantial temperature differences between optical and acoustic phonons (ΔT_{OA}) in various nanostructures upon laser irradiation. Generally, characterizations of interfacial thermal resistance (R''_{tc}) at the nanoscale are difficult and depend on Raman-probed temperature measurements, which only reveal optical phonon temperature information. Here it is shown that ΔT_{OA} for supported monolayer WSe_2 can be as high as 48% of the total temperature rise revealed by optothermal Raman methods—a significant proportion that can introduce sizeable error to R''_{tc} measurements if not properly considered. A frequency energy transport state-resolved Raman technique (FET-Raman) along with a 3D finite volume modeling of 2D material laser heating is used to extract the true interfacial thermal resistance R''_{tc} (determined by acoustic phonon transport). Additionally, a novel ET-Raman technique is developed to determine the energy coupling factor G between optical and acoustic phonons (on the order of 10^{15} W m^{-3} K^{-1}). This work demonstrates the need for special consideration of thermal nonequilibriums during laser–matter interactions at the nanoscale.

1. Introduction

Over the last decade, Raman spectroscopy has proven to be a powerful spectroscopic approach to understanding the fascinating and complex world of energy transport at the nanoscale. A variety of Raman-based methods have been developed to measure the thermal properties of 2D materials and other nanosized structures. Optothermal Raman methods are frequently used to determine interfacial thermal resistance (R''_{tc}) and thermal conductivity (k) of atomically thin materials such as graphene and transition metal dichalcogenides (TMDs).[1–4] This technique involves simultaneous laser heating of the sample and Raman signal characterization. Temperature-dependent Raman signals and a 3D heat conduction model are used to extract thermal property measurements. Raman thermometry through Joule heating similarly probes interfacial energy transport and thermal conductivity; by substituting an electrical current heating source for laser heating, physical modeling, and temperature dependent Raman signals can be used to determine R''_{tc}.[5,6] Another comprehensive optothermal Raman method using continuous wave and pulsed lasers has recently been designed to measure the thermal properties of 2D materials.[7] This method was used to measure the k of monolayer and multilayer graphene by comparing the different Raman temperature responses from a range of laser spot sizes and pulse durations. Furthermore, two-laser Raman thermometry and dual-wavelength flash Raman mapping have been used to measure the thermal conductivity of 2D materials and nanowires, respectively.[8,9]

As powerful as Raman-based approaches are at thermal characterization of nanomaterials, the nonequilibrium optical and acoustic phonon temperature distribution caused by a laser heating source complicates the experimental analysis of Raman temperature information. Raman scattered light gives an indication of the temperature of optical phonons (OPs). It has been shown through a first principles approach that OPs can be responsible for up to 20% of a thin film material's thermal conductivity at the nanoscale.[10] However, even at the atomic scale, acoustic phonons (APs) remain the primary carriers of

N. Hunter, H. Zobeiri, X. Wang
Department of Mechanical Engineering
2025 Black Engineering Building
Iowa State University
Ames, IA 50011, USA
E-mail: xwang3@iastate.edu

N. Azam, M. Mahjouri-Samani
Department of Electrical and Computer Engineering
Auburn University
Auburn, AL 36849, USA
E-mail: mzm0185@auburn.edu

N. Van Velson
Research and Development Department
Advanced Cooling Technologies
Inc.
1046 New Holland Ave., Lancaster, PA 17601-5688, USA
E-mail: nathan.vanvelson@1-act.com

The ORCID identification number(s) for the author(s) of this article can be found under https://doi.org/10.1002/admi.202102059.

DOI: 10.1002/admi.202102059

heat and contribute more to the material's thermal conductivity. Therefore, large temperature differences between OPs and APs can lead to underestimated k predictions. The strong nonequilibrium between optical and acoustic phonon branches must be fully considered for a comprehensive understanding of heat conduction at the nanoscale.

Recent modeling and experimental results suggest that laser-induced heating of nanostructured materials results in significant nonequilibrium between different phonon branches. Lu et al. integrated phonon branch-resolved electron–phonon coupling factors into a multitemperature model to show that significant nonequilibrium exists between different phonon branches in laser irradiated single layer graphene.[11] Waldecker et al. developed a nonthermal lattice model that considers nonequilibrium phonon distributions in laser-excited nm-thick aluminum samples.[12] Dolleman et al. presented an experimental method to measure the thermal nonequilibrium between in-plane and flexural acoustic phonons in locally heated suspended graphene.[13] Their work showed that total in-plane acoustic phonon temperature rises can reach as low as 20% of the flexural acoustic phonon temperature rise and sometimes as high as 370%. Falcão et al. uncovered considerable nonthermal optical phonon populations in semiconductor nanocrystals during photoexcitation experiments through Raman signal analysis.[14]

Overall, very little experimental work has been invested in probing the nonequilibrium phonon dynamics of 2D materials. Recently, Wang et al. employed a nanosecond energy transport state-resolved Raman (ET-Raman) technique to distinguish the optical and acoustic phonon temperatures in photoexcited suspended nm-thick materials (MoS_2, $MoSe_2$, and graphene paper).[15] For the first time, the relative temperature rise contributions of OPs and APs were resolved. Additionally, the energy coupling factor between the two branches was determined and shown to align closely with modeling results. Based on the proven proportionality of laser intensity to optical–acoustic phonon temperature difference ΔT_{OA} (see previously cited paper for explanation), this ns ET-Raman method determined that ΔT_{OA} contributes more to the Raman-observed temperature rise with smaller laser spots (more than 25% for a laser radius of ≈0.4 μm). Additionally, Zobeiri et al. directly characterized the thermal nonequilibrium between in-plane optical phonons modes and acoustic modes of suspended graphene paper (GP) using a Raman-based approach after having precisely determined the thermal conductivity of the GP sample.[16] The determined coupling factor was in good agreement with the predicted values from the phonon-branch resolved multitemperature model developed by Ruan's group.[11,17]

These recent characterizations of nonequilibrium optical–acoustic phonon distributions in suspended 2D materials offer promising insight into nanoscale energy transport during laser–matter interactions. However, this same nonequilibrium phenomenon in supported 2D materials has yet to be experimentally measured due to the complexity of physical factors involved during laser heating. In-plane heat conduction, hot carrier diffusion, and interfacial energy transport become more prominent factors in the Raman-measured thermal response for 2D materials supported on substrates. The cross-plane thermal transport hinders the ability to distinguish the effect of OP and AP temperatures. The previous two methods cited above circumvent this problem by avoiding most cross-plane thermal transport all together by suspending the sample. In the supported case, more of the energy transport is governed by heat conduction across the 2D material–substrate interface. Therefore, a new experimental method must be developed to properly investigate the laser-induced thermal nonequilibrium of optical and acoustic phonons in supported 2D materials.

This work experimentally characterizes the nonequilibrium optical and acoustic phonon distribution in monolayer WSe_2 supported by fused silica substrate during laser heating. A new physical principle is developed to distinguish the temperatures of optical and acoustic phonons. The temperature difference between OPs and APs is reported as a percentage of the total optical phonon temperature rise measured through Raman signal analysis. Using these experimental results alongside a 3D finite volume simulation of the laser heating, the energy coupling factor G between OPs and APs is determined. Additionally, the frequency energy transport state-resolved Raman (FET-Raman) method is used to determine the interfacial thermal resistance R''_{tc} between the monolayer and substrate using the true acoustic phonon temperature information.

2. Distinguish the Optical and Acoustic Phonon Temperatures of Supported Monolayer WSe_2

2.1. Physics Development

Laser irradiation causes the nonequilibrium nature of phonon transport in 2D materials. A laser heating source incident on a semiconducting material excites three primary energy carriers: hot carriers (electron (e)–hole (h) pairs), optical phonons, and acoustic phonons. When the laser excitation energy is equal to or greater than the material bandgap, electrons in the material absorb the photon energy and are brought to a higher energy level in the conduction band. This process creates electron–hole pairs; electrons diffuse quickly and then recombine with holes across the bandgap on the order of nanosecond or less.[18] Thus, excited electrons contribute little to the material's measured thermal conductivity. During electron–hole recombination, electrons transfer their energy to optical phonons through scattering. The energy cascade continues as each optical phonon decays into two acoustic phonons in a process known as anharmonic coupling. The anharmonic coupling between OPs and APs can be characterized by an energy coupling factor G with units W m^{-3} K^{-1}. The energy coupling factor gives a measure of the degree to which thermal energy in the form of OPs converts to thermal energy as APs.

Here it is worth noting that energy coupling between optical and acoustic phonon branches often varies between the three different phonon modes inherent to each branch: longitudinal (LO/LA) and transverse (TO/TA) phonons representing in-plane vibrations and flexural phonons (ZO/ZA) representing cross-plane vibrations. Because monolayer WSe_2 (samples studied in this work) yields a degenerate Raman signal near 260 cm^{-1} that represents both the A_{1g} (out-of-plane vibrational mode) and $E_{2g}{}^1$ (in-plane vibrational modes), the sample material thermal

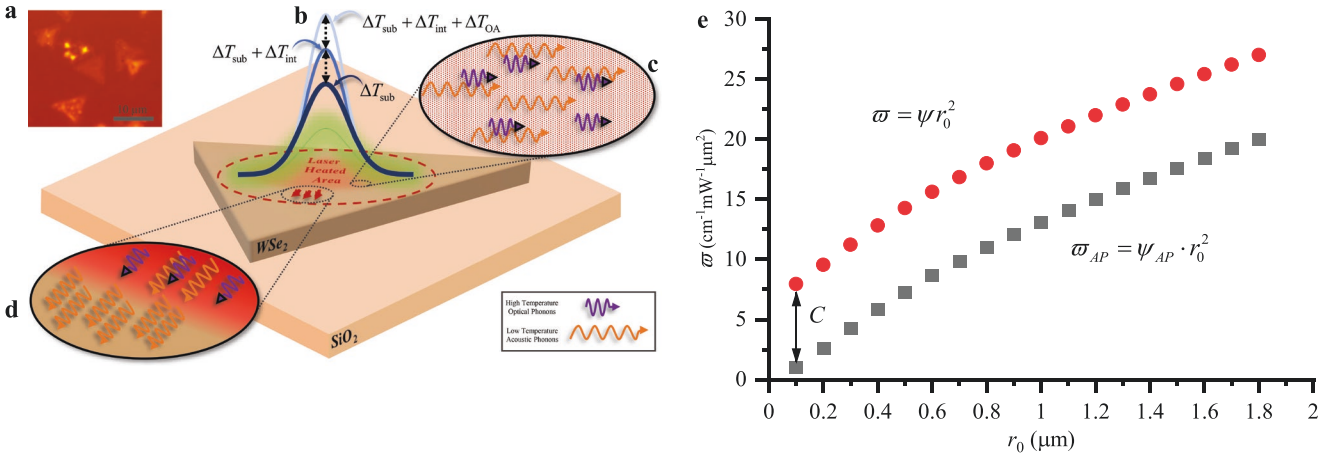

Figure 1. a) Optical image of the WSe_2 monolayer sample. b) Illustration of the Raman-probed temperature rise decomposed into its constituent parts ΔT_{OA}, ΔT_{int}, and ΔT_{sub}. c) Inside the laser heated area, the thicker wave packets represent higher temperature optical phonons. The thinner wave packets represent lower temperature acoustic phonons. d) At the edge of the laser heated area, only acoustic phonons diffuse outside the laser spot. e) The modeling results for a trilayer MoS_2 (just for case of study) on SiO_2 substrate under 1 mW laser irradiation. The simulated Raman measurement is based on the E^1_{2g} mode (LO/TO phonon) with an optical–acoustic phonon energy coupling factor of 4×10^{14} W m^{-3} K^{-1}. This clearly proves the physics idea discussed here: when $r_0 \to 0$, ϖ_{AP} approaches 0 and ϖ reaches a constant C. Finally, under unit laser power irradiation, at any spot size, the $\Delta\overline{T}_{OA}$ contribution to ψ is $\psi_{OA} = C/r_0^2$.

property information extracted from the Raman signal will not distinguish the varying contributions from different phonon branches.[19] Instead, the measured thermal nonequilibrium will indicate generalized temperature differences between all branches of optical phonons and all branches of acoustic phonons.

Throughout the series of energy transfer, different thermal nonequilibriums exist between the respective energy carriers. The Gaussian-shaped 532 nm wavelength laser beam induces similarly shaped temperature distributions for APs and OPs (therefore, the corresponding ΔT_{OA} will also be Gaussian-shaped). As shown in **Figure 1**, within the laser heated area, both high temperature optical and low temperature acoustic phonons diffuse through the sample. The OPs will have shorter lifetimes (ps timescale), very small velocity, and low specific heat compared with APs.[10,20] Thus, their contribution to overall heat conduction is minimal. Outside of the laser spot area, APs will be the primary energy carriers as there is no light source to generate hot carriers. The APs will carry heat laterally toward the edge of the sample as well as transversally across the interface toward the SiO_2 substrate.

As discussed previously, the supported 2D material requires special consideration when assessing the various contributions to material temperature rise during photoexcitation. First, an experimental measurement of the optical phonon temperature rise effect must be determined. In our case, we will measure a parameter called the Raman shift power coefficient (RSC), which will be denoted as ψ. The RSC is defined as a laser power differential of the Raman signal: by increasing the laser power incident on the sample (ΔP), the 2D material experiences a temperature jump and subsequent Raman signal redshift ($\Delta\omega$). By tracking the amount of redshift and laser power change we can define the RSC as $\psi = \Delta\omega/\Delta P = \partial\omega/\partial P$. Details about the exact process of determining the RSC are involved in the next section. Note that ψ represents the Raman intensity weighted average temperature rise of OPs for unit laser power irradiation and can be decomposed into three separate parts: 1) the temperature rise at the surface of the SiO_2 substrate denoted as ΔT_{sub}; 2) the temperature difference between the surface of the substrate and the supported 2D material denoted as ΔT_{int}; and 3) the overall temperature difference between OPs and APs denoted as ΔT_{OA}. Therefore, we can establish a proportionality for the RSC written as $\psi \propto \Delta T_{sub} + \Delta T_{int} + \Delta T_{OA}$. The decomposition of the RSC into its constituent parts is further illustrated in Figure 1b. Note that the AP contribution to the temperature rise is encompassed in both ΔT_{sub} and ΔT_{int}.

The next step in developing a strategy to distinguish the optical–acoustic phonon temperature difference for supported 2D materials requires an examination of the laser spot size effect on the three temperature rise contributions listed above. The substrate thermal resistance R_S governs the temperature rise at the surface and can be defined using the appropriate shape factor for heat conduction through a disk with radius r_0 as $R_S \sim 1/[4(r_0 + \Delta r)k_s]$ where k_s is the substrate thermal conductivity and Δr accounts for enlargement of the heating area due to in-plane heat conduction and hot carrier diffusion.[21] Thus, the corresponding temperature rise ΔT_{sub} is proportional to $1/(r_0 + \Delta r)$.

The total interface resistance R_T between the substrate and the 2D material contributes to the temperature rise ΔT_{int}. The total interface resistance is simply defined using the interfacial thermal resistance R''_{tc} [W^{-1} m^2 K] and laser heating area: $R_T \sim R''_{tc}/[\pi(r_0 + \Delta r)^2]$. Note this parameter R''_{tc} will be solved for using the frequency energy transport Raman technique (FET-Raman) which will be discussed in the next section. Therefore, we can establish that ΔT_{int} is proportional to $1/(r_0 + \Delta r)^2$.

The final temperature rise component in the experimentally measured ψ consists of the temperature difference between optical and acoustic phonons ΔT_{OA}. This temperature effect follows the r_0^{-2} dependency of the laser spot intensity (a thorough justification for this dependency is proven in our previous work[15]). This can be explained by the rapid series of energy

transfer between energy carriers: first, electrons passing energy to OPs, then OPs quickly decaying into APs. Both hot electrons and OPs have little time to diffuse outside of the laser heating spot. Experimental work confirms that electron–hole diffusion has a negligible contribution to heat conduction.[22] Similarly, while OPs will carry some thermal energy away from the laser heated area, the vast majority will be carried away by APs. Thus, the spatial energy distribution of the initial laser intensity will be maintained by the OP–AP temperature difference. In other words, the local temperature difference between optical and acoustic phonons is proportional to the absorbed laser energy at any location under the laser heating area. Consequently, we can write the resulting proportionality as $\Delta T_{OA} \propto I \propto r_0^{-2}$. With these proportionalities established, we can rewrite the Raman shift coefficient ψ as a function of the laser spot radius and arbitrary proportionality constants: $\psi = A/(r_0+\Delta r)+B/(r_0+\Delta r)^2+C/r_0^2$.

At this point, we define a new parameter $\varpi = \psi r_0^2$. This parameter represents the Raman wavenumber shift under unit laser peak intensity (the peak intensity of the Gaussian distribution) and is termed Raman shift intensity coefficient. We can now write $\varpi = Ar_0^2/(r_0+\Delta r)+Br_0^2/(r_0+\Delta r)^2+C$ where the acoustic phonon temperature rise is encompassed in the first two terms $\varpi_{AP} = Ar_0^2/(r_0+\Delta r)+Br_0^2/(r_0+\Delta r)^2$ and the optical–acoustic phonon temperature difference is represented as $\varpi_{OA} = \psi_{OA} r_0^2 = C$. As clearly shown by plotting the relationship between ϖ and r_0 in Figure 1e, ϖ_{AP} approaches zero as $r_0 \to 0$. At the same time, as $r_0 \to 0$ the new parameter ϖ reaches a constant value C (shown as the vertical double-sided arrow in the figure), which represents the exact contribution of the optical–acoustic phonon temperature difference ΔT_{OA}.

A rigorous 3D finite volume model of the thermal energy transport in trilayer MoS_2 on SiO_2 substrate establishes the soundness of this method in isolating and defining the ΔT_{OA} contribution to overall temperature rise. In the simulated laser heating of the sample–substrate system and subsequent Raman signal generation a 1 mW unit laser power irradiation with unity absorption is assumed. This numerical modeling determines the acoustic phonon temperature rise. Then, the Raman peak of the MoS_2 E_{2g}^1 mode corresponding to in-plane vibrations (LO/TO phonon modes) and its associated optical–acoustic phonon energy coupling factor (taken as 4×10^{14} W K^{-1} m^{-3}) is used to calculate optical phonon temperature. Figure 1e shows the simulation results by illustrating the relationship between laser spot radius and the newly defined parameters ϖ and ϖ_{AP}. As shown in Figure 1e, ϖ_{AP} approaches zero as $r_0 \to 0$. However, ϖ approaches a finite value (i.e., the intercept denoted as C). Thus, the intercept C gives a numerical value that can be used to evaluate the overall contribution of ΔT_{OA} in the experimentally measured ψ.

For this experiment, multiple objective lenses were used (20 ×, 50 ×, 100 ×) to obtain ψ values at different laser spot radii. It is important to note here that this process requires normalization of ψ values before plotting. The 20 × RSC value $\psi_{20\times}$ is used as the normalization factor. This step is further detailed in Section 2.2. The resulting ϖ values (i.e., ψr_0^2) were plotted against laser spot radius to determine the constant C. The subsequent RSC value representing the optical–acoustic phonon temperature difference can then be written as $\psi_{OA} = C/r_0^2$. Therefore, an acoustic phonon temperature rise contribution will be written as $\psi_{AP} = \psi - C/r_0^2$. Finally, the respective contributions of the optical phonon and acoustic phonon temperature rises can be accurately distinguished for different sized laser spot scenarios.

2.2. Experimental Results and Discussion

The WSe_2 monolayer samples were fabricated on a fused silica substrate using the laser-assisted synthesis technique (LAST) developed by Azam et al.[23] Stoichiometric WSe_2 powder was placed inside a graphite crucible and the fused silica substrates were placed 6 mm above the crucible. The crucible was laser heated with a continuous wave (CW) CO_2 laser. As the WSe_2 powder evaporated, monolayers formed on the surface of the fused silica substrates (optical image of monolayers shown in Figure 1a). Our previous work exploring the radiative recombination efficiency of monolayer WSe_2 further characterizes the quality and thickness of the monolayer samples used in this work. Atomic force microscopy measurements confirm a ≈0.7 nm sample thickness.[24] Annular dark-field scanning transmission electron microscope imaging and photoluminescence mapping done by Azam et al. further examined the quality, defect density, and stoichiometry of monolayers fabricated using the LAST method.

A 532 nm CW laser was focused on the monolayer samples using a confocal Raman spectroscopy setup. Three different objective lenses were used to vary the laser spot size on the sample: 20 × ($r_0 \approx 2.0$ μm), 50 × ($r_0 \approx 0.9$ μm), and 100 × ($r_0 \approx 0.6$ μm). In each case, a range of laser powers was used to simultaneously heat the sample and excite a Raman signal. The laser power range was carefully chosen so as to avoid sample damage while still generating a strong Raman signal peak shift for the WSe_2 monolayer at 260 cm^{-1}. **Figure 2**a–c shows the 2D Raman intensity contours for a representative sample (sample #2) at each objective lens demonstrating the obvious degenerate A_{1g} and $E_{2g}{}^1$ peaks throughout the respective incident laser power ranges.

Multiple Raman spectra were collected at room temperature while increasing the laser power. The Raman signals were fitted using a Gaussian curve and the peak locations of the fitted curves were used to measure the amount of redshift. Fitted Gaussian curves for a representative sample are shown in **Figure 3**b. This figure depicts the essential components of the experimentally measured RSC—namely, $\Delta\omega$ and ΔP. As shown in Figure 2d,f, the Raman peak locations are plotted against the corresponding incident laser power and a linear fitting is applied. The RSC is simply defined as the slope of this fitted line (i.e., $\partial\omega/\partial P$). This experimentally obtained ψ is a numerical value that represents the Raman intensity weighted average temperature rise of optical phonons within the laser heated area of the monolayer sample. It is worth noting that ψ obtained from CW laser heating is proportional to interfacial thermal resistance R''_{tc}, Raman temperature coefficient $\partial\omega/\partial T$ (i.e., a measure of how the Raman signal depends on material temperature), and laser absorption α. Both $\partial\omega/\partial T$ and α are highly sample-specific parameters that introduce non-negligible sources of error into final measurements.[25] The ET-Raman method circumvents these potential errors through

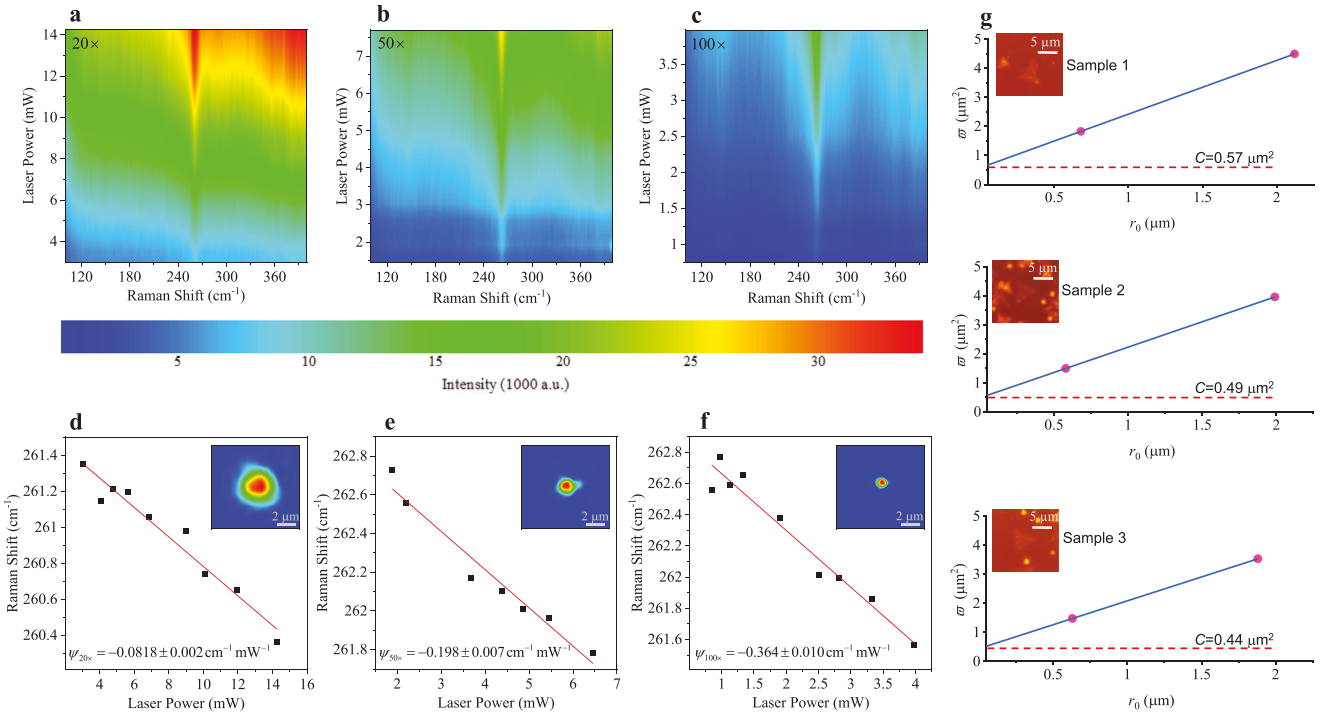

Figure 2. a–c) Raman intensity contours highlighting the evident WSe_2 peak near 260 cm^{-1} for all three objective lenses. d–f) Plots showing the linear relationship between Raman signal peak location and laser power. The slope of the linear fitting is the experimentally measured Raman shift coefficient ψ. The top right insets are spatial energy distributions of the laser spot on the monolayer sample for all three objective lenses. g) A linear fitting of the $(r_0, \Omega\, r_0^2)$ experimental data points shows the y-intercept value which numerically quantifies the temperature difference between optical and acoustic phonons.

a ratio analysis approach which creates a normalized RSC value where Raman temperature coefficient and laser absorption effects have been cancelled out. In our case, three distinct energy transport states are created by varying the size of the laser heated area with the three different objective lenses. The 20 × RSC value is used as the reference so that our normalized RSC values can be written as such $\Omega_{20\times} = \psi_{20\times}/\psi_{20\times}$, $\Omega_{50\times} = \psi_{50\times}/\psi_{20\times}$, and $\Omega_{100\times} = \psi_{100\times}/\psi_{20\times}$.

The normalized RSC values are used to create the new parameter $\varpi = \psi r_0^2$ (i.e., ψ becomes the normalized values of 1, $\Omega_{50\times}$, and $\Omega_{100\times}$, respectively, for the three objective lenses). The new parameter ϖ functions as a tool to provide an experimental characterization of ΔT_{OA}; as r_0 approaches zero, the intercept value C allows us to derive an RSC for the optical–acoustic phonon temperature difference as $\psi_{OA} = C/r_0^2$. The relationship between ϖ and r_0 can be approximated as linear when the heated area enlargement term Δr is small enough. It is worth noting that the linear assumption will not hold true for smaller laser spot sizes where nonlinear effects become more prominent. As the laser spot size approaches 0, the relationship between ϖ and r_0 would need to be adjusted to account for the nonlinearity. However, since this experimental work involves laser spot sizes that fall within the window of linearity as shown in Figure 1e (i.e., $r_0 \geq 0.6$ μm), the linear approximation is sufficient. Only two data points are needed for the linear fitting that determines the C intercept. Using the results from the 20 × and 100 × objective lenses guarantee sufficiently distinguished energy transport since the laser spot size difference is largest between these two objectives. Thus, a linear fitting is applied to the two data points defined as $(r_{20\times}, \varpi_{20\times})$ and $(r_{100\times}, \varpi_{100\times})$ to find the resulting intercept C. The fitting and resulting C value for all three samples are shown in Figure 2g.

It should be noted that including the data point for the 50 × objective—$(r_{50\times}, \varpi_{50\times})$—would have been preferred for linear fitting. However, stage drift and small focal depths made it difficult to guarantee consistent and distinct laser spot sizes incident on the ≈1 nm samples for the 100 × and 50 × objectives. Rather than being twice as large as the laser spot formed by the 100 ×, the 50 × laser spot was ≈50% larger. Therefore, including the 50 × objective data resulted in unnecessary uncertainty in the final C determination. While more data points for this fitting would be ideal, the limitations of our confocal Raman system prohibited further interpolation. Nevertheless, the two data points used for the linear fitting still provide sufficient detail to determine a C intercept value that accurately approximates the contribution of the optical–acoustic phonon temperature difference.

After C has been determined, the original ψ (which was experimentally determined via ET-Raman) can be broken down into its constituent parts. As shown in Figure 3a, ψ represents the temperature rise of optical phonons (ΔT_{OP}) which consists of ΔT_{AP} and ΔT_{OA}. Recall that both ΔT_{OA} and ΔT_{AP} can be represented using the experimentally determined ψ and fitted value C as $\psi_{OA} = C/r_0^2$ and $\psi_{AP} = \psi - C/r_0^2$. Therefore, for each laser spot size, the respective contributions of ΔT_{AP} and ΔT_{OA} can be evaluated. For the three samples measured, the acoustic

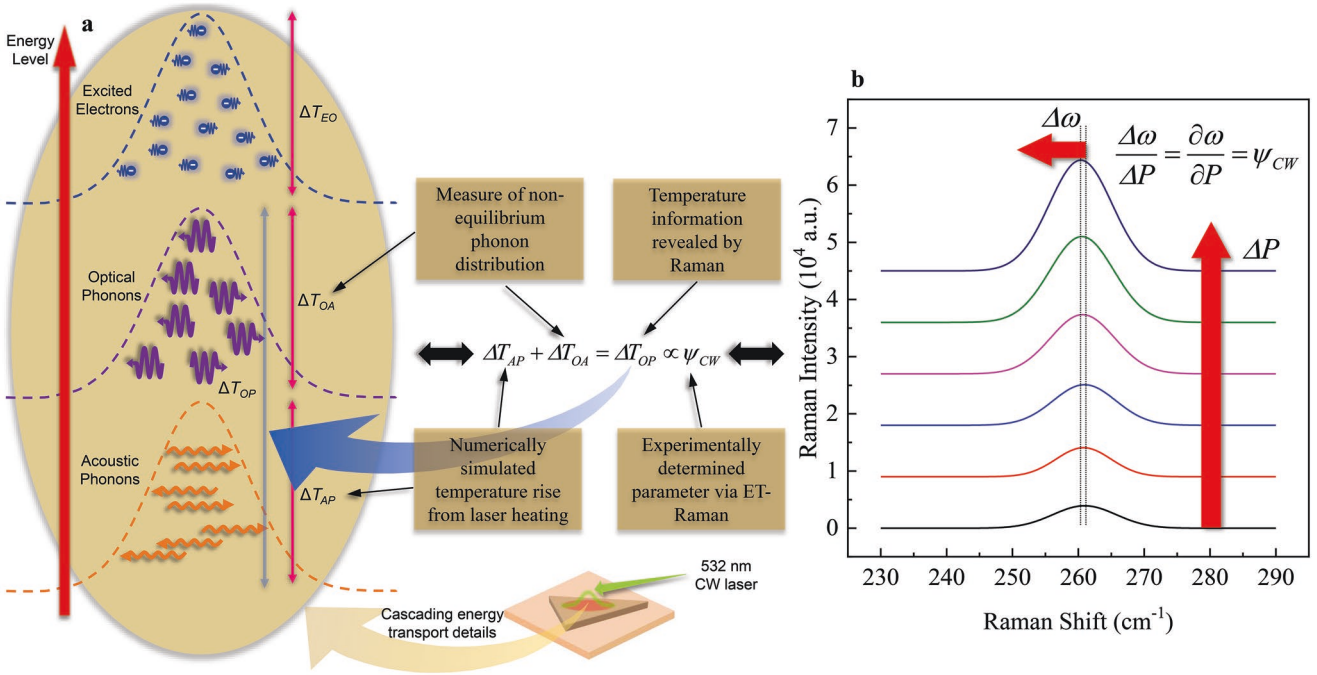

Figure 3. a) Illustration of the nonequilibrium energy carrier distribution during laser heating in the monolayer sample. Excited electrons transfer energy to optical phonons rapidly after initial excitation. These high energy optical phonons are detected during Raman measurements. Then optical phonons transfer energy to acoustic phonons. The acoustic phonon temperature rise is calculated via numerical modeling. b) The experimentally determined Raman shift coefficient ψ_{CW} is determined by measuring the red-shifted WSe_2 Raman signal with increasing laser power. This parameter is proportional to the optical phonon temperature rise ΔT_{OP}.

phonon temperature rise and the optical–acoustic temperature difference are shown as percentage contributions to the total Raman temperature rise ΔT_{OP} in **Figure 4**.

As shown in the figure, the ΔT_{OA} contribution to Raman-measured temperature rise decreases as the laser spot size increases across all three samples. In the case of monolayer WSe_2, when the laser spot radius reaches 0.6 µm, the ΔT_{OA} can contribute up to 48% of the Raman-measured temperature rise. On the other hand, with larger laser spot sizes (i.e., 2.0 µm for the 20 × objective), ΔT_{OA} will more likely contribute around 15% of the optical phonon temperature rise. The large variation in percentage contribution of temperature differences across different laser spot sizes suggest that high energy densities correspond to greater nonequilibrium between optical and acoustic phonons. As the laser spot decreases, the absorbed energy intensity per unit volume incident on the sample increases. This higher energy density means that the cascading energy transfer that starts with photoexcited electrons is concentrated in a smaller volume. In other words, more excited electrons, and consequently more optical phonons that receive those electrons' energy, are concentrated in a smaller volume. Thus, the natural nonequilibrium from photoexcitation between optical and acoustic phonons is enhanced. Raman-based experimental methods using smaller laser spots must consider this phonon nonequilibrium in data processing. If neglected, this optical–acoustic phonon temperature difference could lead to significant underestimations of thermal conductivity and interface thermal conductance.

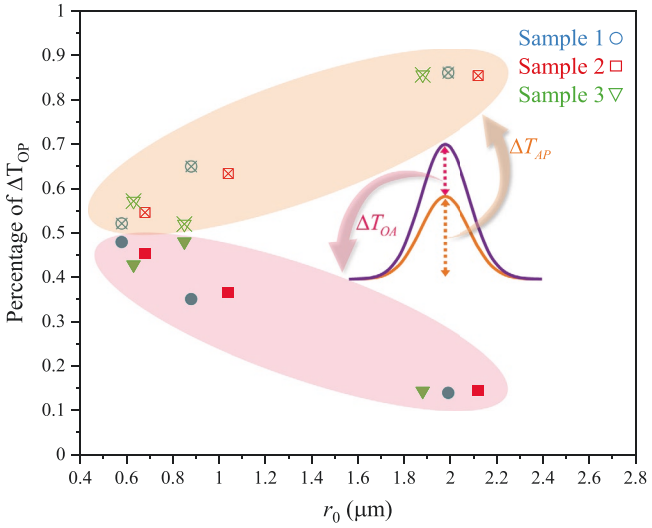

Figure 4. The percentage breakdown of the component temperature rises for each sample. The total temperature rise is represented by the optical phonon temperature ΔT_{OP} revealed by Raman experiments. The temperature difference between optical and acoustic phonons ΔT_{OA} increases as the laser spot size reduces and can reach up to 48% under the 100 × objective lens. Conversely, the acoustic phonon temperature ΔT_{AP} makes up a majority of ΔT_{OP} as the laser spot size increases.

The inverse relationship between ΔT_{OA} and laser spot size revealed by these Raman experiments matches closely with the relationship found for other supported 2D materials investigated by our lab.[26] In recently published work, it was found that ΔT_{OA} could contribute as much as ≈45% of the total OP temperature rise measured by Raman for nm-thick MoS_2 supported on quartz substrate when the laser spot radius is

reduced to 0.5 µm. Neglecting this nonequilibrium could lead to over-predictions of interfacial thermal resistance by as much as 100%. Therefore, conclusive experimental results confirm the existence of substantial optical–acoustic phonon thermal nonequilibrium during Raman-based measurements of supported nanoscale 2D materials.

3. Intrinsic Interface Thermal Resistance/Conductance

Frequency domain energy transport state-resolved Raman (FET-Raman) is an experimental technique involving a single CW laser source modified by an amplitude modulator. By modulating the amplitude of the CW laser heating source at a specified frequency and measuring the thermal response in the 2D material, it becomes possible to also measure the interfacial thermal resistance R''_{tc} between the monolayer WSe_2 and fused silica substrate. Generating a square wave modulation of the laser introduces a reduced thermal diffusion into the fused silica substrate. In other words, the energy transport into the sample–substrate system is distinct from the steady-state CW laser heating case. FET-Raman resolves the thermal transport at the interface by comparing the Raman response from amplitude-modulated sample heating to that of steady-state heating. This is done by creating a normalized RSC out of the two differentiated Raman responses (i.e., $\Omega_{FR/CW} = \psi_{FR}/\psi_{CW}$). A 3D finite volume numerical model simulates the acoustic phonon temperature rises in both heating cases to create a theoretical RSC Ω_{sim} that can be equated to the experimental $\Omega_{FR/CW}$. Comparison of theoretical and experimental values allows for precise determination of the interfacial thermal resistance. This technique has been used in the past to measure the thermal conductivity of suspended nm-thick $MoSe_2$.[27]

FET-Raman depends on creating distinct energy transport phenomena that can be interpreted in the different thermal responses of the sample via Raman spectroscopy. The key physical principles of the two unique heating scenarios in the experimental setup are shown in **Figure 5**a. In the CW laser heating case, heat conduction into the substrate can be treated as infinite (since steady-state heating ensures that thermal energy continuously diffuses in the cross-plane direction through the monolayer and into the fused silica substrate). This infinite thermal diffusion length can be approximated as 10 × the laser spot size and is denoted in the figure as L_T.

In this case of steady-state heating, the substrate thermal resistance $R_{S,CW}$ can be evaluated using the formula $R_{S,CW} = \Delta R_1 + \int_{r_0}^{20r_0} [2\pi k_S r^2]^{-1} dr$ where the upper limit of integration $20r_0$ denotes 10 × the laser spot diameter, k_S is the substrate thermal conductivity, and r_0 is the laser spot radius. Note that the ΔR_1 term accounts for heating area resistance within a hemisphere centered at the substrate surface that extends into the substrate a length equal to the laser spot radius r_0. The justification for estimating the infinite thermal diffusion length during CW heating as 10 × the laser spot diameter can be explained by the following: using the appropriate shape factor for heat conduction of a disk with diameter D through a semi-infinite medium with thermal conductivity k, the thermal resistance can be described as $R = 1/2Dk$. This thermal resistance can be broken down into two terms and written in the integral form as shown above: $R = \Delta R_1 + \int_{r_0}^{\infty} [2\pi k r^2]^{-1} dr$. The integral term accounts for the thermal resistance beyond the laser spot radius penetration into the substrate and has an upper limit of integration of infinity to indicate the infinite thermal diffusion length. Evaluating these two separate thermal resistances, it can be shown that $R_{S,CW}$ is ≈97% of R proving that the approximation of L_T as 10 × the laser spot diameter is valid.

Using the thermal diffusion length approximation and a laser spot radius of 2 µm, evaluating the integral results in $R_{S,CW} = 5.4 \times 10^4$ K W^{-1}. It is easily shown that the magnitude of $R_{S,CW}$ dwarfs that of the total interface resistance defined as $R_T \sim 4R''_{tc}/\pi D^2$. Therefore, in this steady-state case, the temperature rise induced by $R_{S,CW}$ disproportionately impacts the overall thermal transport in the sample–substrate system effectively masking the heating effect at the interface.

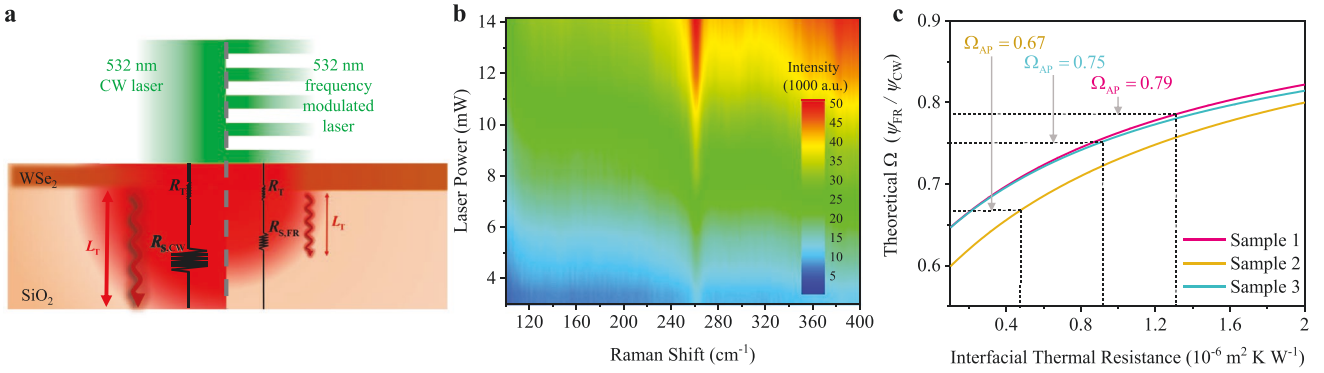

Figure 5. a) Illustration of the heat conduction physics in the monolayer-substrate system after CW and amplitude-modulated laser irradiation. Note the disproportionate impact of the substrate thermal resistance during CW heating compared to the more moderate substrate resistance during amplitude-modulated laser heating. b) The 2D Raman intensity contour at different modulated laser powers in the wavenumber range of interest shows the characteristic WSe_2 Raman signal near 260 cm^{-1}. c) The plotted curves represent the ratio of the frequency laser heating temperature rise to the CW laser heating temperature rise evaluated through numerical modeling. The experimentally measured ratio Ω_{exp} is corrected to Ω_{AP} which accounts for the true acoustic phonon temperature difference between 2D material and substrate. The evaluated Ω_{AP} is used to determine the interfacial thermal resistance.

However, in the amplitude-modulated heating case, a reduced thermal diffusion length into the fused silica substrate decreases the substrate thermal resistance and allows for more sensitive detection of thermal transport at the interface. A square-wave modulated laser with modulation frequency f induces heating such that the thermal diffusion length can be written as $L_T = \sqrt{\pi\alpha_\perp / f}$ where $\alpha_\perp$ is the cross-plane thermal diffusivity of the substrate. Using reference values for the volumetric heat capacity and thermal conductivity of glass ($\rho c_p = 1.65 \times 10^6$ J m^{-3} K^{-1} and $k_S = 1.4$ W m^{-1} K^{-1})[21] $\alpha_\perp$ can be evaluated as 8.5×10^{-7}m^2 s^{-1}. Therefore, using a frequency of 100 kHz, L_T for the amplitude-modulated laser heating case can be approximated as 5.2 µm. The substrate thermal resistance $R_{S,FR}$ can be evaluated using the same spherical coordinates integral formula as the CW case. Setting the upper limit of integration as L_T = 5.2 µm, the integral evaluates to $R_{S,FR} = 3.5 \times 10^4$K W^{-1}. Thus, $R_{S,FR}$ is only 65% of $R_{S,CW}$. This reduced substrate resistance means R_T contributes more to the sample–substrate heating. Therefore, the interfacial thermal resistance R''_{tc} becomes more sensitive to precise measurement.

It is worth noting again that the unique quality of FET-Raman comes from its ability to make precise nanoscale thermal measurements without the need of Raman temperature coefficient $\partial\omega/\partial T$ and laser absorption α parameters. By creating a normalized RSC $\Omega_{FR/CW}$ as the ratio ψ_{FR}/ψ_{CW}, the sample-specific $\partial\omega/\partial T$ and α are cancelled out. It should also be noted that the 3D finite volume model simulates a Raman intensity weighted average temperature rise; because of the Gaussian-shaped spatial energy distribution of the irradiating laser, the Raman scattered light leaving the laser spot area must be weighted proportionally. In the CW case, this average can be written as a spatial integral $\overline{T}_{CW} = \int_0^V Ie^{-\Delta z/\tau_L} T \mathrm{d}v / \int_0^V Ie^{-\Delta z/\tau_L} \mathrm{d}v$ where I is the Gaussian-distributed CW laser intensity, T is the material temperature, Δz is the distance from the sample surface, and τ_L is the material's characteristic absorption depth for the given laser wavelength of 532 nm. The laser intensity can be expanded as $I = I_0 \exp(-r^2/r_0^2)\exp(-\Delta z/\tau_L)$ where I_0 is the peak laser intensity (assumed to be 1 mW for modeling) and r_0 is the laser spot radius measured during Raman experiments to make the simulation match the experimental conditions as closely as possible. In the amplitude-modulated case, the Raman weighted average includes a temporal integral as well and becomes $\overline{T}_{FR} = \int_0^t \int_0^V Ie^{-\Delta z/\tau_L} T \mathrm{d}v\mathrm{d}t / \int_0^t \int_0^V Ie^{-\Delta z/\tau_L} \mathrm{d}v\mathrm{d}t$.

Both Raman-weighted integrals can be evaluated as $\overline{T}_{CW(FR)} = aR''_{tc} I_0/2 + \overline{T}_{s,CW(FR)}$ where $\overline{T}_{s,CW(FR)}$ represents the simulated acoustic phonon temperature rise (Raman intensity weighted) at the substrate surface under CW and amplitude-modulated heating, respectively. The laser absorption α is assumed to be unity (a valid assumption because of the ratio analysis eliminating the laser absorption effect). Note that the atomic-scale thickness of the WSe_2 monolayer (≈0.7 nm) makes proper modeling of the 2D material extremely computationally expensive as the mesh size would be pushed to the sub-nm region. Consequently, our 3D model simulates the substrate temperature rise $\overline{T}_{s,CW(FR)}$, and the analytical formula shown above is used to calculate the 2D layer temperature rise $\overline{T}_{CW(FR)}$. Now, the equivalency of the theoretical temperature rise ratios (i.e., $\Omega_{sim} = \overline{T}_{FR}/\overline{T}_{CW}$) and the normalized experimental RSC (i.e., $\Omega_{exp} = \psi_{FR}/\psi_{CW}$) can be used to solve for R''_{tc}.

Furthermore, now that it has been determined that the laser spot size can severely influence the proportional contribution of ΔT_{OA} to the total Raman measured temperature rise, the FET-Raman method requires special consideration of the objective lens used. Since our numerical model only simulates ΔT_{AP}, we must choose an objective with a larger laser spot size to reduce the impact of a relatively large ΔT_{OA}. As shown previously, the 20 × objective produces a laser spot with a diameter around 4 µm. At this size, the ΔT_{OA} contribution is less than 20% of the ΔT_{OP} revealed by Raman. Additionally, a larger laser spot is preferred because as laser spot size decreases the hot carrier diffusion and in-plane phonon transport become more pronounced.[28] Thus, larger laser spots will minimize the impact of these variables on the interfacial thermal resistance measurement.

As shown in Figure 5b, the 2D Raman intensity contour at the 20 × objective for periodic square-wave heating shows a similar profile to that of the CW heating case along the same irradiating laser power range. As detailed earlier, the Raman signal peak locations are plotted against laser power and a linear fitting is applied to yield the RSC for the amplitude-modulated case. Using sample #1 as a representative sample, the RSC values are $\psi_{CW,20\times} = -0.082 \pm 0.002$ cm^{-1} mW^{-1} and $\psi_{FR,20\times} = -0.066 \pm .001$ cm^{-1} mW^{-1} resulting in a normalized RSC of $\psi_{FR,20\times}/\psi_{CW,20\times} = \Omega_{exp} = 0.81 \pm 0.03$. However, this normalized RSC represents the ratio of Raman-probed optical phonon temperature rises. Only the energy transport of acoustic phonons across the interface characterizes the true interfacial thermal resistance. Additionally, the 3D finite volume model simulates the acoustic phonon temperature rise. Therefore, the RSC values can be replaced with the recently determined acoustic phonon RSC values defined as $\psi_{AP} = \psi - C/r_0^2$. Substituting these CW and amplitude-modulated ψ_{AP} values for the 20 × objective case results in an acoustic phonon normalized RSC which evaluates to $\Omega_{AP} = 0.79 \pm 0.05$.

This experimentally determined acoustic phonon RSC is equated to the theoretical RSC composed of the ratio of evaluated Raman-weighted integrals from before. This equivalency can be written as $\Omega_{AP} = \frac{\overline{T}_{FR}}{\overline{T}_{CW}} = \frac{aR''_{tc} I_0/2 + \overline{T}_{s,FR}}{aR''_{tc} I_0/2 + \overline{T}_{s,CW}}$. Assuming a theoretical 1 mW incident laser irradiation that is fully absorbed, the interfacial thermal resistance can now be solved. For sample #1, the simulated acoustic phonon temperature rises of the substrate evaluate to $\overline{T}_{s,CW} = 15.9$ K and $\overline{T}_{s,FR} = 9.9$ K resulting in $R''_{tc} = 1.31 \times 10^{-6}$ m^2 K W^{-1}. Figure 5c shows graphical results of the R''_{tc} for all three samples. The plotted curves represent the theoretical RSC $\Omega_{sim} = \overline{T}_{FR}/\overline{T}_{CW}$ for a trial range of R''_{tc} values. Mapping the acoustic phonon RSC Ω_{AP} to the plotted curve identifies the unique interfacial thermal resistance for a given sample. The full numerical R''_{tc} results with corresponding uncertainties are shown in **Table 1**.

The R''_{tc} values found in this work range from 0.48×10^{-6} to 1.32×10^{-6} m^2 K W^{-1}. The modest range of measured values can be attributed to material structural differences between samples. As extensively detailed in our previous work, Raman peak analysis of the 260 cm^{-1} degenerate vibrational modes of these

Table 1. The Raman shift laser power coefficients (RSC) for the CW and amplitude-modulated cases. Both OP and AP normalized RSC values are listed along with the corresponding interfacial thermal resistance using the AP normalized RSC.

Sample number	ψ_{CW} [cm^{-1} mW^{-1}]	ψ_{FR} [cm^{-1} mW^{-1}]	Ω_{exp}	Ω_{AP}	R''_{tc} [10^{-6} m^2 K^1 W^{-1}]
1	− 0.082 ± 0.002	− 0.066 ± 0.001	0.81 ± 0.03	0.79 ± 0.05	1.32 ± 0.52
2	− 0.093 ± 0.003	− 0.066 ± 0.002	0.71 ± 0.03	0.67 ± 0.05	0.48 ± 0.24
3	− 0.095 ± 0.002	− 0.073 ± 0.004	0.77 ± 0.03	0.75 ± 0.04	0.93 ± 0.38

WSe_2 monolayer samples reveals the unique structural characteristics between samples. The variation in peak intensity, line width, and Raman shift location suggest distinctive qualities. Specifically, differences in peak intensity indicate distinct interfacial spacing between 2D material and substrate; light entering from the bottom of the 2D material will reflect off the top surface of the substrate and undergo multiple reflections within this interfacial gap. The reflected light interferes with the measured Raman signal causing Raman intensity enhancement. Therefore, the varying peak intensities between samples indicate varying atomic-scale size differences in the interfacial gaps. Consequently, heat conduction across these unique interfaces will also be affected.

The measured values in this work align closely with a picosecond ET-Raman study previously done in our lab for a similar TMD 2D material on glass substrate.[29] For nm-thick MoS_2 layers ranging from 1.8 to 18 nm, the interfacial thermal resistance was found to be on the order of 2×10^{-6} m^2 K W^{-1}. However, the R''_{tc} results of this current study are one order of magnitude larger than the results from our previous work investigating the photoluminescence quantum yield (PL QY) and R''_{tc} of the same WSe_2 monolayers on fused silica substrate.[24] Using the nanosecond (ns) ET-Raman method, the interfacial thermal resistance was found to range from 0.63×10^{-7} to 4.8×10^{-7} m^2 K W^{-1} across five unique monolayer samples. It is worth identifying the possible reasons for this order of magnitude difference in R''_{tc} measurements.

One obvious reason for the resulting differences comes from inherent differences in the experimental techniques of FET-Raman and ns ET-Raman. As opposed to periodic square-wave heating where CW laser exposure on the monolayer surface can be up to 5 µs, the ns laser irradiates the sample with pulses where each pulse has a width of 200 ns and time between pulses is 3 µs. Thus, the unique temporal natures of the two heating sources create distinctive thermal responses in the monolayer-fused silica samples. For example, the thermal diffusion length into the substrate during ns laser heating is only 0.8 µm—approximately 15% of the diffusion length during amplitude-modulated heating. Additionally, for the respective laser powers used in each experiment, the energy delivered to the sample during a single ns laser pulse is ≈2 × greater than the energy delivered over the same time during CW heating. The dissimilar heating effects caused by the two heating sources will inevitably create different temperature rises in the sample. The main distinction between these two heating scenarios is the larger hot carrier concentration generated during ns laser heating due to the higher peak laser intensity relative to the CW laser. More electron–hole pairs imply increased scattering events with phonons. This increased scattering and high population of electron–hole pairs could help facilitate energy coupling at the interface of the 2D material and substrate. Thus, the smaller interfacial thermal resistance measured from our previous work could be explained by the enhanced interface energy coupling caused by photoexcitation from the ns laser.

The enhanced measurement sensitivity of the ns ET-Raman method also explains the different experimental R''_{tc} results. As thoroughly detailed in recent work, it has been shown that the ET-Raman method optimizes the sensitivity for precise R''_{tc} measurements as the ns pulsing laser minimizes its pulse width.[30] Reduced pulse widths will shrink the thermal diffusion length into the substrate and similarly shrink the magnitude of the substrate thermal resistance. In this way the temperature difference across the interface becomes more measurable. Thus, the square-wave periodicity of the FET-Raman experiment with µs timescale pulse widths will not be able to achieve the same level of sensitivity as the ns ET-Raman method.

4. Energy Coupling Factor between Optical and Acoustic Phonons

Using the previously evaluated ΔT_{OA} and ΔT_{AP} percentage contributions to total optical phonon temperature rise revealed by Raman experiments, we can now determine the phonon–phonon coupling factor (G) between OPs and APs. It is known that the local temperature difference between OPs and APs is proportional to the absorbed laser energy at any given point under the laser spot area. This has been clearly justified and explained in our previous work.[15] Representing the absorbed laser power as I_a [mW m^{-2}], this temperature difference can then be written as $\Delta T_{OA} = I_a/G\Delta z$ where $1/G$ [m^{-3} K^{-1} W] represents the coupling factor proportionality constant and the $1/\Delta z$ factor accounts for the thickness component of the laser heated volume in the WSe_2 monolayer. Note that I_a only considers the absorbed laser energy within the monolayer. Thus, I_a will only be a fraction of the total laser power incident on the WSe_2 surface (I); the absorbed energy term can be expanded as $I_a = I(1-e^{-\Delta z/\tau_L})$ where $e^{-\Delta z/\tau_L}$ represents the laser intensity attenuation as the light travels through the monolayer thickness Δz. Accounting for the Gaussian-shaped laser beam with radius r_0, the laser intensity I is written as $I = I_0 \exp(-r^2/r_0^2)$ where $I_0 = 1\ mW/\pi r_0^2$ is the laser power per unit heating area. Note I_0 is the one after considering all the optical interference effect within the monolayer WSe_2, including the forward and backward propagating laser intensity. Also since the monolayer is extremely thin, it is physically reasonable to treat I constant across the layer. This significantly simplifies the physical model development outlined below.

Under this formulation, the OP–AP temperature difference becomes $\Delta T_{OA} = I(1-e^{-\Delta z/\tau_L})/G\Delta z$. However, this is only a local temperature difference meaning that this ΔT_{OA} is true for any given point (r, z) under the laser heating area. The next step involves transforming the local temperature difference formula into the Raman intensity weighted average temperature difference $\Delta\overline{T}_{OA}$. This weighted average reflects the fact that the Raman scattering from the WSe_2 monolayer is proportional to the Gaussian-shaped laser intensity. Thus, after uniting the percentage contribution of ΔT_{OA} determined via experimental RSC values with the analytical equation formulated above, the Raman-intensity weighted average optical–acoustic temperature difference is $\Delta\overline{T}_{OA} = \cdot\int \Delta T_{OA}\cdot I\cdot 2\pi r dr / \int I\cdot 2\pi r dr$. Evaluating this integral using the experimentally measured laser spot radius r_0, the Raman weighted OP–AP temperature difference becomes $\Delta\overline{T}_{OA} = I_0(1-e^{-\Delta z/\tau_L})/2\Delta z G$.

The final step involves rewriting $\Delta\overline{T}_{OA}$ in terms of already established experimental and simulated results. Recall that $\psi_{OA} = C/r_0^2$ was the first quantitative representation of the OP–AP temperature difference where C was the interpolated intercept value from ET-Raman experiments at multiple objective lenses and r_0 was the experimentally measured laser spot radius. Similarly, the experimental quantity representing the AP temperature difference could be written as $\psi_{AP} = \psi - C/r_0^2$ where ψ was the RSC value determined via ET-Raman measurements. Therefore, the amount of OP–AP temperature difference as a percentage of total AP temperature rise can be written simply as a new parameter $\gamma = \psi_{OA}/\psi_{AP}$. Note that the denominator of this ratio is the effective acoustic phonon temperature rise and not the Raman measured optical phonon temperature rise. For the representative sample #1, each objective lens results in a unique γ value: $\gamma_{20\times} = 0.140$, $\gamma_{50\times} = 0.351$, and $\gamma_{100\times} = 0.479$. It is worth emphasizing that these experimentally determined values are Raman intensity weighted numerical representations of ΔT_{OA} and ΔT_{AP} (i.e., $\Delta\overline{T}_{OA}$ and $\Delta\overline{T}_{AP}$). In other words, this new parameter defines an equivalency such that $\gamma = \psi_{OA}/\psi_{AP} = \Delta\overline{T}_{OA}/\Delta\overline{T}_{AP}$. Hence, it is possible to substitute $\Delta\overline{T}_{OA}$ with $\Delta\overline{T}_{AP}\cdot\gamma$ where $\Delta\overline{T}_{AP}$ is the simulated acoustic phonon temperature rise of the 2D layer evaluated from 3D finite volume modeling of laser heating. The coupling factor can now be solved for as $G = I_0(1-e^{-\Delta z/\tau_L})/(2\cdot\Delta z\cdot\Delta\overline{T}_{AP}\cdot\gamma)$.

Solving for G, the resulting coupling factors for sample #1 at each objective lens are found to be 3.17×10^{15} (20×), 1.77×10^{15} (50×), and 1.45×10^{15} W m^{-3} K^{-1} (100×). The resulting G values and the corresponding uncertainties for all three samples can be found in **Table 2**. The determined coupling factors align closely with those found in recent work from Zobeiri et al. investigating the nonequilibrium phonon distributions in laser heated nm-thick MoS_2 layers on quartz substrate.[26] However, because nm-thick MoS_2 provides both E_{2g} (TO/LO phonon modes) and A_{1g} (ZO phonon mode) Raman signals, the in-plane OP–AP coupling factor was distinguished from the cross-plane one. As stated previously, for monolayer WSe_2 these same two vibrational modes appear as a degenerate single Raman peak near 260 cm^{-1}. Therefore, the resulting G represents the energy coupling between all optical phonon branches (TO/LO/ZO) with all acoustic phonon branches (TA/LA/ZA). In the case of supported nm-thick MoS_2, the resulting total G between all OPs and all APs is on the order of $\approx10^{15}$ W m^{-3} K^{-1}—the same magnitude as the G for supported monolayer WSe_2.

These determined coupling factors for supported 2D materials are one magnitude larger than those determined for suspended MoS_2 and $MoSe_2$.[15] The larger OP–AP energy coupling for the supported cases could be attributed to increased phonon–phonon scattering. As detailed in the work of Lu et al., G can be defined in terms of volumetric heat capacity C_p and phonon relaxation time τ_p as the equation $G = C_p/\tau_p$.[11] From molecular dynamics simulations, it is known that both acoustic and optical phonon relaxation times in 2D materials are reduced drastically when going from suspended to supported.[31] In other words, the average time interval between phonon collisions is reduced (i.e., more phonon–phonon scattering). Therefore, the lower phonon relaxation times for the supported WSe_2 monolayers imply higher G values. Furthermore, supported samples allow heat conduction through the interface and into the substrate. Therefore, they require higher laser powers to reach the same acoustic phonon temperature as suspended 2D materials. The increased laser intensity will generate more e–h pairs, which imply greater nonequilibrium between OPs and APs due to increased phonon scattering events.

5. Conclusion

An optothermal Raman technique was developed to measure the thermal nonequilibrium induced by photoexcitation of monolayer WSe_2 supported on a fused silica substrate. For the first time, the temperature difference between optical and acoustic phonons was characterized as a percentage of the Raman-probed temperature rise for a supported monolayer material. The findings align closely with previous experimental works showing that decreasing the laser spot size generates greater nonequilibrium between OPs and APs as hot carrier diffusion and in-plane heat conduction become more pronounced. The substantial ΔT_{OA} can reach as high as 48% of the total OP temperature rise leading to significant error in Raman-based thermal property measurements if not properly considered. Additionally, after determining the true acoustic phonon temperature rise induced by laser heating, the interfacial thermal resistance R''_{tc} was measured via FET-Raman. The R''_{tc} results from this work ($\approx1\times10^{-6}$ m^2 K^1 W^{-1}) match closely with those

Table 2. The energy coupling factor G for three WSe_2 monolayer samples determined for each objective lens.

Sample number	$G_{20\times}$ [10^{15} W m^{-3} K^{-1}]	$G_{50\times}$ [10^{15} W m^{-3} K^{-1}]	$G_{100\times}$ [10^{15} W m^{-3} K^{-1}]
1	3.17 ± 0.14	1.77 ± 0.11	1.45 ± 0.08
2	4.09 ± 0.20	2.60 ± 0.12	2.62 ± 0.16
3	3.70 ± 0.14	1.62 ± 0.08	2.02 ± 0.08

for other supported 2D TMD materials on glass substrates. Lastly, for the first time, the energy coupling factor G between OPs and APs was measured for a supported monolayer 2D material and found to be on the order 10^{15} W m^{-3} K^{-1}.

Acknowledgements

N.H., N.A., and H.Z. contributed equally to this work. The authors gratefully acknowledge support in part by the National Science Foundation (CBET1930866 and CMMI2032464).

Conflict of Interest

The authors declare no conflict of interest.

Data Availability Statement

The data that support the findings of this study are available from the corresponding author upon reasonable request.

Keywords

2D interfacial energy transport, interfacial thermal resistance, phonon transport, Raman probing, thermal nonequilibrium

Received: October 20, 2021
Revised: December 3, 2021
Published online:

[1] W. Cai, A. L. Moore, Y. Zhu, X. Li, S. Chen, L. Shi, R. S. Ruoff, *Nano Lett.* **2010**, *10*, 1645.
[2] E. Yalon, Ö. B. Aslan, K. K. H. Smithe, C. J. McClellan, S. V. Suryavanshi, F. Xiong, A. Sood, C. M. Neumann, X. Xu, K. E. Goodson, T. F. Heinz, E. Pop, *ACS Appl. Mater. Interfaces* **2017**, *9*, 43013.
[3] X. Zhang, D. Sun, Y. Li, G.-H. Lee, X. Cui, D. Chenet, Y. You, T. F. Heinz, J. C. Hone, *ACS Appl. Mater. Interfaces* **2015**, *7*, 25923.
[4] X. F. Yue, Y. Y. Wang, Y. Zhao, J. Jiang, K. Yu, Y. Liang, B. Zhong, S. T. Ren, R. X. Gao, M. Q. Zou, *J. Appl. Phys.* **2020**, *127*, 104301.
[5] C.-C. Chen, Z. Li, L. Shi, S. B. Cronin, *Appl. Phys. Lett.* **2014**, *104*, 081908.
[6] Y. Liu, Z.-Y. Ong, J. Wu, Y. Zhao, K. Watanabe, T. Taniguchi, D. Chi, G. Zhang, J. T. L. Thong, C.-W. Qiu, K. Hippalgaonkar, *Sci. Rep.* **2017**, *7*, 43886.
[7] Q.-Y. Li, K. Xia, J. Zhang, Y. Zhang, Q. Li, K. Takahashi, X. Zhang, *Nanoscale* **2017**, *9*, 10784.
[8] J. S. Reparaz, E. Chavez-Angel, M. R. Wagner, B. Graczykowski, J. Gomis-Bresco, F. Alzina, C. M. Sotomayor Torres, *Rev. Sci. Instrum.* **2014**, *85*, 034901.
[9] A. Fan, Y. Hu, H. Wang, W. Ma, X. Zhang, *Int. J. Heat Mass Transfer* **2019**, *143*, 118460.
[10] Z. Tian, K. Esfarjani, J. Shiomi, A. S. Henry, G. Chen, *Appl. Phys. Lett.* **2011**, *99*, 053122.
[11] Z. Lu, A. Vallabhaneni, B. Cao, X. Ruan, *Phys. Rev. B* **2018**, *98*, 134309.
[12] L. Waldecker, R. Bertoni, R. Ernstorfer, J. Vorberger, *Phys. Rev. X* **2016**, *6*, 021003.
[13] R. J. Dolleman, G. J. Verbiest, Y. M. Blanter, H. S. J. van der Zant, P. G. Steeneken, *Phys. Rev. Res.* **2020**, *2*, 012058.
[14] B. P. Falcão, J. P. Leitão, M. R. Correia, M. R. Soares, H. Wiggers, A. Cantarero, R. N. Pereira, *Phys. Rev. B* **2017**, *95*, 115439.
[15] R. Wang, H. Zobeiri, Y. Xie, X. Wang, X. Zhang, Y. Yue, *Adv. Sci.* **2020**, *7*, 2000097.
[16] H. Zobeiri, N. Hunter, R. Wang, T. Wang, X. Wang, *Adv. Sci.* **2021**, *8*, 2004712.
[17] A. K. Vallabhaneni, D. Singh, H. Bao, J. Murthy, X. Ruan, *Phys. Rev. B* **2016**, *93*, 125432.
[18] S. Mouri, Y. Miyauchi, M. Toh, W. Zhao, G. Eda, K. Matsuda, *Phys. Rev. B* **2014**, *90*, 155449.
[19] W. Zhao, Z. Ghorannevis, K. K. Amara, J. R. Pang, M. Toh, X. Zhang, C. Kloc, P. H. Tan, G. Eda, *Nanoscale* **2013**, *5*, 9677.
[20] A. S. Bandyopadhyay, C. Biswas, A. B. Kaul, *Beilstein J. Nanotechnol.* **2020**, *11*, 782.
[21] F. P. Incropera, D. P. DeWitt, *Introduction to Heat Transfer*, John Wiley & Sons, New York **2002**.
[22] H. Zobeiri, R. Wang, Q. Zhang, G. Zhu, X. Wang, *Acta Mater.* **2019**, *175*, 222.
[23] N. Azam, Z. Ahmadi, B. Yakupoglu, S. Elafandi, M. K. Tian, A. Boulesbaa, M. Mahjouri-Samani, *2D Mater.* **2020**, *7*, 015014.
[24] N. Hunter, N. Azam, H. Zobeiri, R. Wang, M. Mahjouri-Samani, X. Wang, *ACS Appl. Mater. Interfaces* **2020**, *12*, 51069.
[25] S. Xu, A. Fan, H. Wang, X. Zhang, X. Wang, *Int. J. Heat Mass Transfer* **2020**, *154*, 119751.
[26] H. Zobeiri, N. Hunter, N. Van Velson, C. Deng, Q. Zhang, X. Wang, *Nano Energy* **2021**, *89*, 106364.
[27] H. Zobeiri, R. Wang, T. Wang, H. Lin, C. Deng, X. Wang, *Int. J. Heat Mass Transfer* **2019**, *133*, 1074.
[28] P. Yuan, R. Wang, T. Wang, X. Wang, Y. Xie, *Phys. Chem. Chem. Phys.* **2018**, *20*, 25752.
[29] P. Yuan, H. Tan, R. Wang, T. Wang, X. Wang, *RSC Adv.* **2018**, *8*, 12767.
[30] N. Hunter, H. Zobeiri, T. Wang, X. Wang, *Int. J. Heat Mass Transfer* **2021**, *179*, 121644.
[31] B. Qiu, X. Ruan, *Appl. Phys. Lett.* **2012**, *100*, 193101.